Full scale experimental tests and numerical model validation of reinforced concrete slab subjected to direct contact explosion

Andrew Ruggiero[1], Nicola Bonora[1], Giuseppe Curiale[2], Stefano De Muro[2], Gianluca Iannitti[1], Sonia Marfia[3], Elio Sacco[4], Sara Scafati[2], Gabriel Testa[1]

[1] Department of Civil and Mechanical Engineering, University of Cassino and Southern Lazio, Via G. di Biasio 43, 03043, Cassino, Italy

[2] Protezione Aziendale, Area Tecnica – Rete Ferroviaria Italiana S.p.A., Piazza della Croce Rossa 1, 00161 Italy

[3] Department of Engineering, University of Roma Tre, Via Vito Volterra 62, 00146, Rome, Italy

[4] Department of Structures in Engineering and Architecture, University of Naples Federico II, Via Claudio 21, 80125, Naples, Italy

Abstract

In this work, a numerical model for analyzing the mechanical behavior of a reinforced concrete slab subjected to a direct contact explosion was developed, using the explicit finite element code LS-DYNA and facing the following issues: generation and propagation of the blast wave, interaction with the solid structure, and mechanical behavior of the slab. The different elements that constitutes the slab were modeled as deformable bodies and the constitutive model coefficients for each material, when not directly measured, were calibrated by comparison with experimental measures. To this purpose, a reinforced concrete slab used for civil buildings was loaded with three different charge of EXEM 100: 2.1, 6.3 and 10.5 kg. For each test, the blast wave pressure-time profile was measured at two different locations and the damage extension in concrete and reinforcing elements was estimated. Using the same sets of material dependent parameters, a good agreement between experimental and numerical results was found for all tested configurations. The validated numerical model provided insight into the role of different structural elements on the failure mechanisms into the slab and is a useful tool for investigating alternative loading configurations and designing potential reinforcement solutions.

Keywords

Blast effects, Concrete slabs, Direct contact explosion, Experimental test, Numerical model.

1. Introduction

The design of concrete structures for blast resistance has been of great interest not only to military agencies but also to the engineering community interested to the effect of explosion due to potential accidents. This case can occur, for instance, in petrochemical industries or in civil buildings subjected to gas explosions. Moreover, explosions are used also for the demolition of undesired or old buildings.

Recent terrorist attacks have pointed out that the public buildings are not safe places in case of explosion. Although the main cause of injuries against people are due to pressures and heat of the explosion, there are other threats that can be hazardous at the same manner. After an explosion, falling debris, breaking windows and, eventually, a partial or complete building collapse are further causes of injuries. With this in mind, the improvement of the blast resistance of buildings means to save lives. This can be achieved designing right countermeasures expressly developed to mitigate the effects of blast loads on buildings in order to reduce the collateral effects of the explosion. Although, there are some design guidelines for the blast resistance, especially in the framework of the military protective structures [1][2], experimental and numerical analyses can be fundamental supports for the design of proper reinforcements for mitigating the blast effects. In fact, several investigations have been developed in the recent literature to evaluate the response of structures subjected to loading conditions characterized by high strain rates and high pressures.

The interest in investigating the effects of blast explosion on the civil constructions has significantly increased in the last years [3][4][5], due to the frequent terroristic attacks. The case of terroristic attack is characterized by the circumstance that explosions might occur inside buildings, representing a very special and interesting problem. On the other hand, while some investigations concerning structures, hit by external explosions, are available in literature [6][7][8][9][10], much less studies have been developed related to in-door explosion. Furthermore, very few investigations of the explosive in direct contact with the structure have been developed. This, also because the experimental campaigns are very expensive, time consuming, and pose serious security problems. In this perspective, numerical analyses can be a powerful tool to reducing these obstacles. Further, they allow gaining insight into the complex failure mechanisms occurring in the slab and not directly observable.

Wang et al. [11] presented close-in explosion experimental tests and numerical simulations of square reinforced concrete slabs. Spall damage at different severities was observed. Shi et al. [12] proposed a study of the influence of explosive shape on the concrete slab spall damage. Their studies demonstrate that increasing the height/diameter ratio of the cylindrical TNT charge, keeping unchanged the mass of the TNT charge, significantly increases the spalling damage of the concrete slab. Other papers present experimental and numerical investigations on concrete slabs with contact explosion, for example [13][14], mainly considering a reduced quantity of the TNT charge.

In order to provide adequate structural protection against blast effects on concrete structures, innovative materials and strengthening techniques have been studied and they are still under development [15]. Among the others, Ohkubo et al. [16] performed contact-explosion tests on concrete plates reinforced by carbon or aramid fiber sheet. They found that fiber sheet reinforcement significantly reduced local spall damage and prevented concrete plates from fragmentation. Li et al. [17] performed contact explosion tests on concrete slabs to investigate the crater dimension and the spall damage. Slabs made of normal strength concrete and of ultra-high performance concrete were tested. Comparing the results of the experimental tests, the better blast resistance capacity of ultra-high performance concrete slabs was verified. Foglar et al. [18] presented the results of full-scale blast experiments on a steel-fiber reinforced concrete full-scale bridge deck. They demonstrated that the blast resistance of reinforced concrete material increased by adding high-performance steel fibers.

Li et al. [19] performed an experimental and numerical study on a composite slab designed in order to obtain high level blast resistance. The matrix of high strength self-compacting concrete was reinforced by conventional rebars and by steel wire meshes that served as further reinforcements. Moreover, steel fibers were added to the concrete cover layer where the tensile cracks locate to provide micro crack-bridging effects. Yoo et al. [20] proposed a study of the impact and blast resistances of ultra-high-performance fiber reinforced concrete.

The ACI report [21], published in 2014, addresses the design of structures to resist to blast effects due to explosions. Specifically, it deals with the determination of the threat, the evaluation of structural loads, the behavior of structural systems and the design of structural elements for new structures or for retrofitting existing ones.

Although some studies have been already proposed, the field of blast- and impact-resistant design still deserves more investigations with the aim of studying the behavior of concrete structures under blast effects and designing innovative reinforcement to mitigate these effects.

The present study aims to investigate in-door blast effects on civil constructions, such as airports, train stations, and other possible sensible objectives. In particular, the interest has been devoted to the analysis of an almost classical reinforced concrete slabs loaded with the charge placed at the center of the upper surface of the structure. A numerical model was developed with the explicit finite element code LS-DYNA and the following issues were addressed: generation and propagation of the blast wave, interaction with the solid structure, and mechanical behavior of the slab. The different elements that constitute the slab were modeled as deformable bodies and the constitutive model coefficients for each material, when not directly measured, were calibrated by comparison with experimental measures.

To this purpose, tests with three different charges of EXEM 100, an explosive commonly used in mines, were performed: 2.1, 6.3, and 10.5 kg. For each test, the blast wave pressure-time profile was measured at two different locations and the damage extension in concrete and reinforcing elements was estimated.

Once set the material dependent coefficients, the numerical model reproduced with good accuracy the features observed in all the tested configurations, providing insight into the role of different structural elements on the failure mechanisms into the slab. Further, the validated model proved to be a useful tool for investigating alternative loading configurations and designing potential reinforcement solutions. In Iannitti et al. [22], the numerical model was used to investigate the influence of partitions (mimicking elements likely present in civil buildings) on the blast action. In Marfia et al. [23], the analysis was deepened by investigating the slabs positioned in a more realistic two floor frame, loaded with two different charges (10.5 and 16.8 kg of EXEM 100), in three different configurations, plain, slabs reinforced with a Kevlar layer, and slabs reinforced with honeycomb panel.

2. Slab structure and methodology

In this section, the experimental tests on reinforced concrete slabs, subjected to contact explosion, are presented. They are part of a wide experimental campaign in which different types of slabs were tested. In the following, the structural elements are described in detail.

2.1. Description reinforced concrete slabs

Reinforced concrete slabs used in the investigation are typical of civil constructions, with dimensions 3600×4000×340 mm^3. They are composed of three preslabs, each one with dimensions 1200×4000 mm^2, as schematically represented in Figure 1. The pre-cast concrete plank of the preslabs is characterized by a thickness of 50 mm and it is reinforced with a square net of ϕ6 mm steel bars at a distance of 150 mm in the two orthogonal directions. Furthermore, a truss with ϕ8 mm and ϕ12 mm bars is present in the longitudinal direction of the preslabs between two adjacent polystyrene blocks. In fact, each preslab contains two polystyrene blocks and three trusses. Over the preslabs the in situ concrete is poured to fill the gaps between two adjacent polystyrene blocks and to create three ribs and a topping with 50 mm thickness, that is reinforced by a ϕ6 mm steel wire net with mesh 150 mm × 150 mm. Then, a waterproofing sheet is placed and, finally, a screed of 100 mm of thickness, made in fiber reinforced concrete, is built. In particular, the fiber reinforced concrete is obtained by adding to the concrete mixture synthetic microfibers with a density of 8 kg/m^3. The fibers are characterized by high mechanical strength that improves the ductility after cracking, the toughness, the impact and fatigue strength, the crack resistance and the freezing and thawing resistance of concrete. The fiber is characterized by a high adherence to the concrete matrix as it is a corrugated with the shape of sinusoidal wave. Inside the fiber reinforced concrete screed a square steel mesh of ϕ6 mm wires with dimensions 150 mm × 150 mm is introduced.

The concrete is characterized by a strength greater than 40 MPa while for the reinforcement the S355JR steel, that has an ultimate strength greater than 450 MPa, was used.

(a)

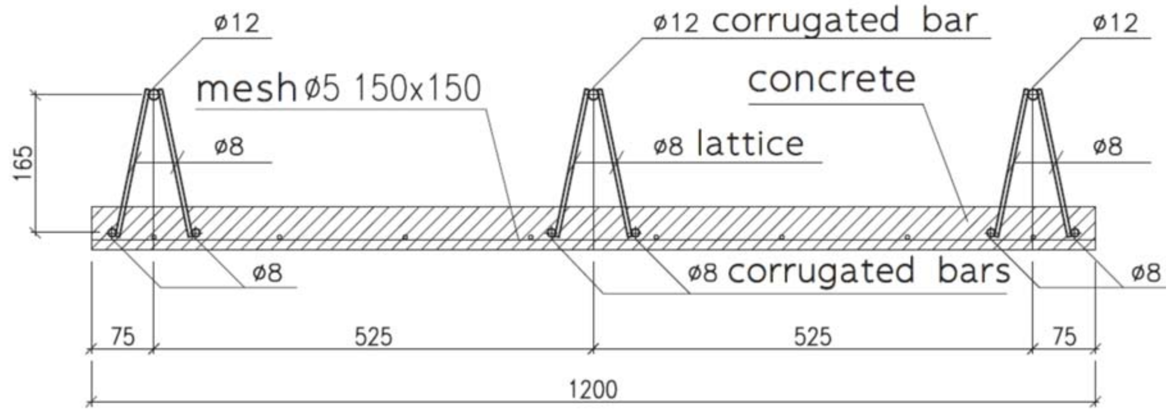

(b)

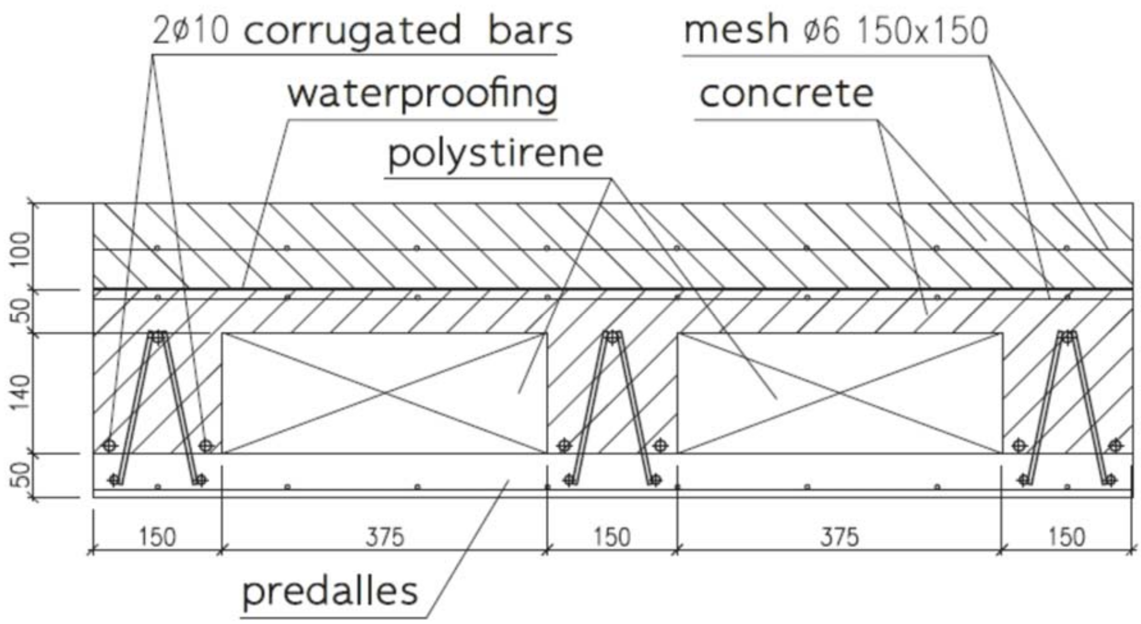

Figure 1: Scheme of the predalle (a) and of the slab (b).

The slab is simply supported on walls with height of 500 mm and width of 370 mm, which are sited on direct foundations. A scheme and a picture of a slab are reported in Figure 2.

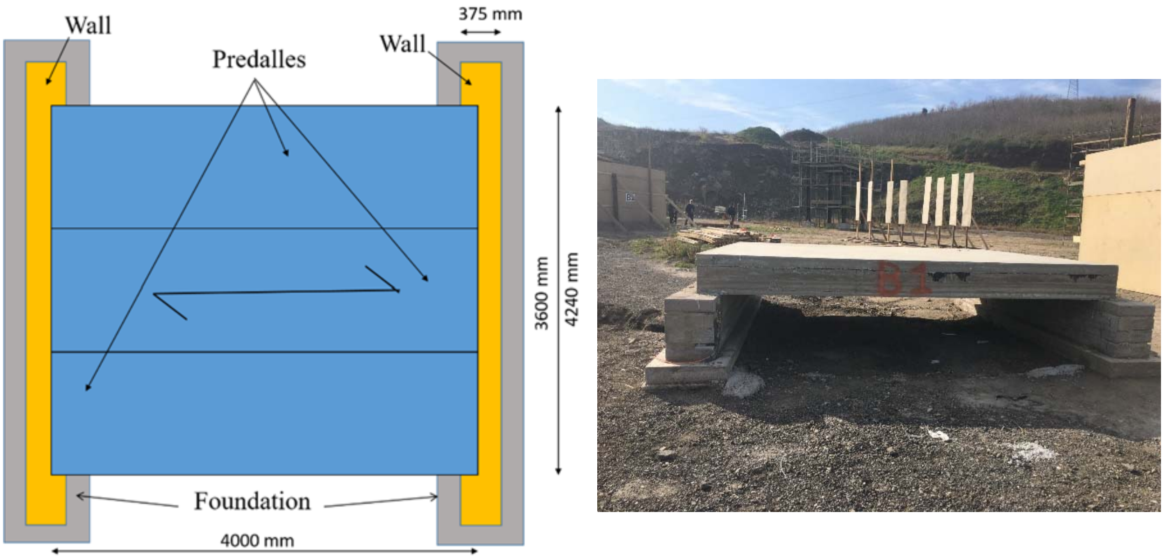

(a) (b)

Figure 2: Slab scheme (a) and picture (b).

2.2. Material characterization

Laboratory tests were performed to characterize the concrete properties. In particular, compressive tests were accomplished on the concrete of the slabs for evaluating the compressive strength, which resulted 44.1 - 48.1 MPa.

For what concerns the fiber reinforced concrete, tests were performed in order to determine the compressive and tensile strength. In particular, compressive and indirect tensile tests on cylindrical specimens with diameter 75 mm and height of 75 mm, according to codes [24], [25] and [26], were performed. The compressive and tensile strengths resulted 19.8 MPa and 2.38 MPa, respectively, corresponding to a reduced value of the strength as a lower class of concrete is adopted for the screed.

2.3. Experimental equipment

In order to measure the pressure wave, two sensors PCB Piezotronics were placed along at the middle of the slab edge at a horizontal distance of 2600 mm. The two sensors were positioned at different heights, one at 300 mm and the other at 1300 mm from the top surface of the slab, as illustrated in **Errore. L'origine riferimento non è stata trovata.**. The different positions of the two sensors allow evaluating the effects on the pressure profiles given by both the distance from the charge and the interaction of the blast wave with the slab.

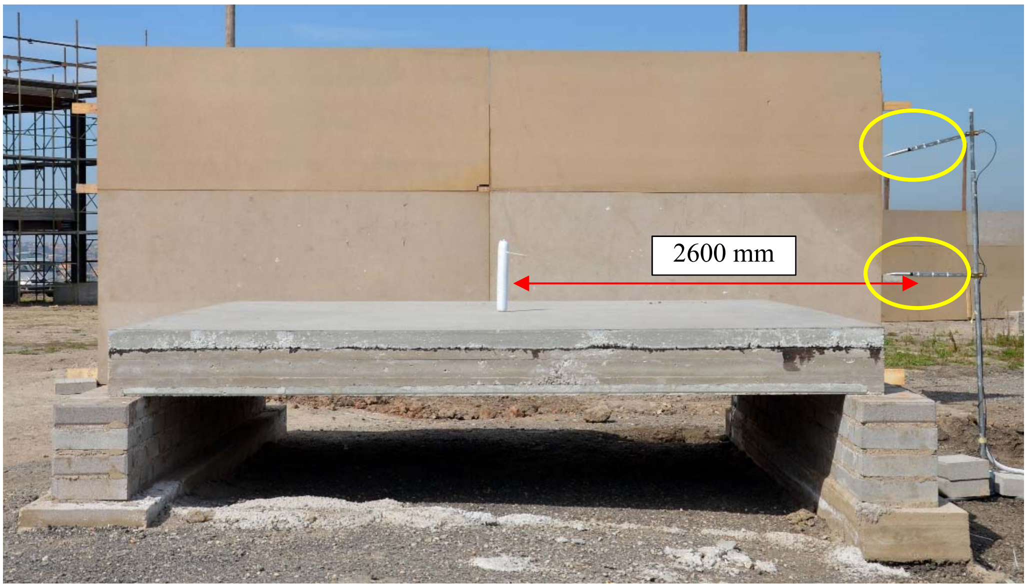

Figure 3: Placement of the pressure sensors.

A 3D laser scanner was also used to obtain the digitalized geometry of the craters after the explosion. The device operates with a maximum range of 187 meters (approx. 600 ft.) and with a data acquisition rate of 1016 million of pixel/sec. In particular, a 3D CAD analysis is carried out adopting a software able to elaborate the 3D point clouds, derived from the 3D scanner, in order to recreate the real geometry of the analyzed object.

Furthermore, a drone pro was used to shoot from the above during the explosions. Finally, two ultra-fast cameras, with a maximum frame rate of 1400000 fps (7500 fps at full resolution) was adopted.

2.4. Explosive

The slabs were subjected to a blast wave generated by the detonation of the explosive EXEM 100. This was supplied in cartridges of 2.10 kg with the following dimensions: diameter of 70 mm, length of 470 mm. The technical characteristics of the explosive are reported in Table 1. The cartridges, in the number of one, three or five, were collocated at the center of the slabs in the vertical position to exploit the resulting symmetries, as in **Errore. L'origine riferimento non è stata trovata.**. The detonator was placed at the top and inserted for about 80 mm. Even when more than one cartridge was used, only one detonator was adopted.

Density	1270	kg/m^3
Detonation velocity	5500	m/s
Detonation energy:		
• Shock	2.30	MJ/kg
• Gas	2.00	MJ/kg
• Total	4.30	MJ/kg
Gas volume (0°C/Atm.)	790	l/kg
Detonation pressure	14300	MPa

Table 1: Technical characteristic of EXEM 100.

3. Experimental configurations and results

Four reinforced concrete slabs, called B1, B2, B3 and B4, were tested with a different amount of explosive. The experiments were performed in the Basalt Pit in Montecompatri, close to Rome (Italy) as part of a wider campaign. In Figure 4 a view of the test location made by the drone is reported.

Figure 4: Test location: View from the Drone

The details of the performed experimental tests on the slabs are reported in Table 2. In the following the experimental results for all the tests are reported and commented.

The scheme of tests 1 and 2, with the exact placement of the cartridge and of the pressure sensors, is illustrated in **Errore. L'origine riferimento non è stata trovata.**. The explosion and the blast wave propagation can be observed in Figure 5, where four images captured by the drone are reported. The significant damage in Test 1 involves only the fiber reinforced screed layer and a circular crater of 223 mm of diameter and 52 mm of depth occurs, as it can be observed in the photo reported in Figure 6(a) and from the crater analysis made from 3D CAD geometry, illustrated in Figure 6(b).

Test	Slab	Explosive (kg)	N. Cartridge	Scheme
1	Slab B2	2.1	1	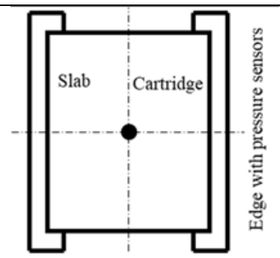
2	Slab B2	2.1	1	
3	Slab B3	10.5	5	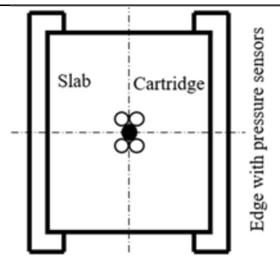
4	Slab B4	10.5	5	
5	Slab B1	6.3	3	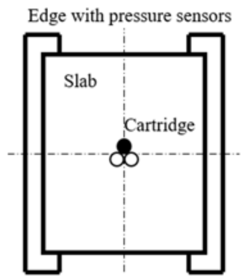

Table 2: Tests on the slabs.

Test 2 is performed again on Slab B2, already tested with test 1; the aim of this second explosion is to get a new measure of the pressure, so the results in terms of damage are not considered, as the slab was already damaged by the explosion of test 1.

Figure 5: Explosion and blast wave propagation of Test 1 (the red dashed line indicates the hockwave front on the ground).

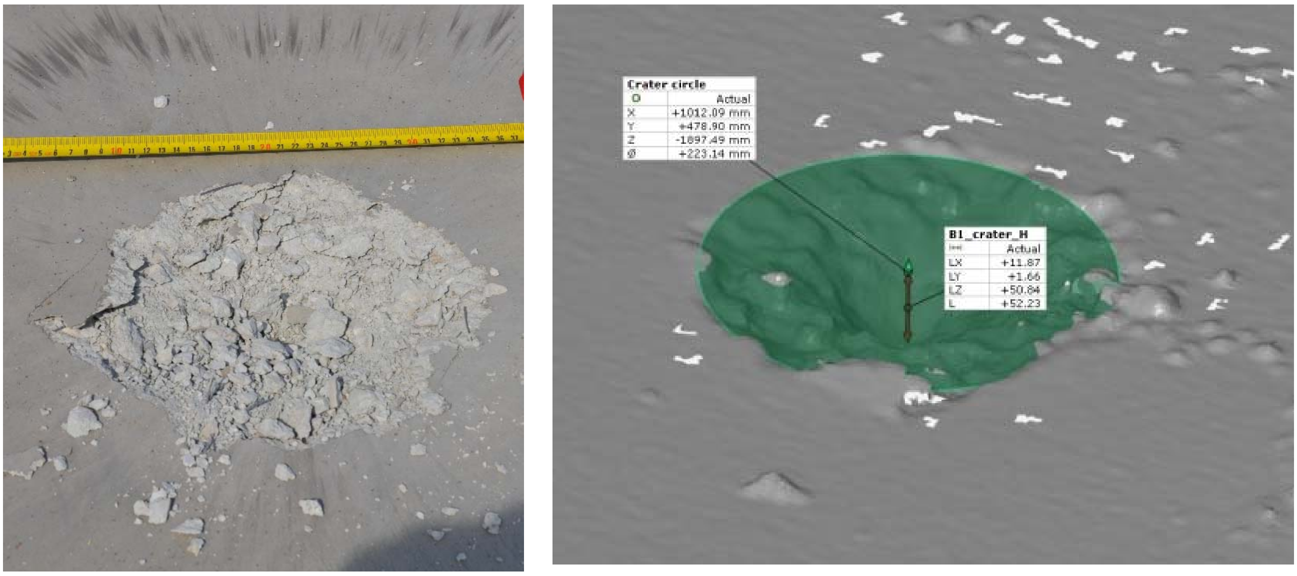

(a) (b)

Figure 6: Crater generated in Test 1: (a) photo; (b) scheme obtained by the 3D CAD analysis

The scheme of test 3 and 4, illustrating the position of the five cartridges for a total amount of 10.5 kg of explosive, is reported in Table 2. In both the tests, the explosion determined a hole crossing all the thickness of the slab with a significant damage of all the layers of the slabs. The dimensions of the holes are similar in the two tests, but their shape is slightly different.

For test 3, the resulted hole has a reverse truncated conical shape. At the slab top, a circular crater, characterized by 620 mm of diameter and illustrated in Figure 7(a), occurred. In Figure 7(b), the crater at the slab bottom is visible. It can be noted the bulging of the preslabs and the failure of some steel bars, placed in the pre-cast concrete plank and in the ribs. Spallation occurred at the slab bottom region, as shown in Figure 7(b), due to the tensile state generated in the concrete deck of the preslabs by the reflected stress wave.

The breach in test 4 presents a cylindrical shape. The crater at the top of the slab is characterized by an elliptical shape with dimension of the axes 540 mm and 610 mm, as illustrated in Figure 8(a). In Figure 8(b) the scheme of the crater at the top of the slab, obtained by the 3D Cad analysis, is reported. The longer axis is placed in the direction of the preslabs. At the bottom of the slab, there is no bulging, but some bars of the preslabs failed as in test 3. In Figure 9 the crater at the bottom and the breach from 3D CAD analysis are reported. The estimated dimensions of the breach axes result 318 mm and 447 mm.

(a)

(b)

Figure 7: Crater generated (a) at the top and (b) at the bottom of the slab in Test 3.

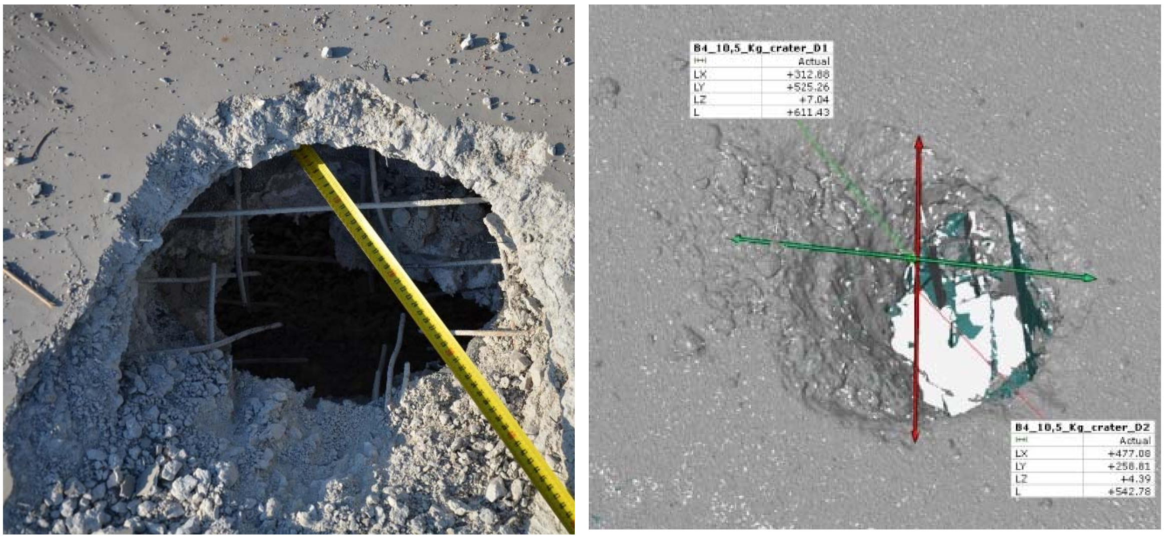

(a) (b)

Figure 8: Crater generated at the slab top in Test 4: (a) photo, (b) scheme obtained by the 3D CAD analysis.

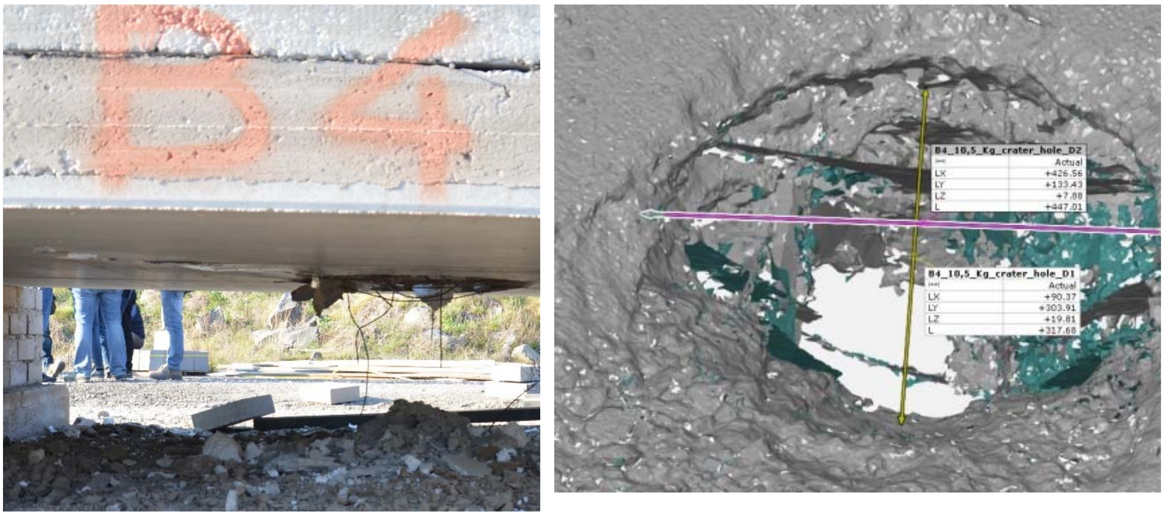

(a) (b)

Figure 9: Test 4: (a)Photo of the crater generated at the slab bottom; (b) Breach scheme from 3D CAD analysis.

The scheme of Test 5 is represented in Table 2. Three cartridges were placed at the center of the slab but only the black one in the figure was triggered. In Figure 10, the explosion and the blast wave propagation can be observed in the three photos, taken from above, by the drone. In this test, a crater at the top of the slab and significant damage at the bottom were generated. Complete breaching did not occur, although the concrete resulted crumbled through the whole thickness of the slab. The irregular shape of the crater shown in Figure 11 is due to the asymmetry of the cartridges with respect to the geometry of the slab. The dimensions in two orthogonal directions are 357 mm and 500 mm with the higher value along the preslabs direction (Figure 12). The hole is almost circular with a diameter of about 150 mm. The area damaged at the bottom of the slab is more extended, as it can be noted in Figure 13. The bars at the bottom of the preslabs are not broken but they are only bent. When the crumbled concrete is removed through the whole thickness, the through hole appears clearly showing failure of reinforcing bars in screed and in-situ concrete (Figure 14).

Figure 10: Explosion and blast wave in Test 5 (the red dashed line indicates the hockwave front on the ground).

Figure 11: Crater generated at the slab top in Test 5.

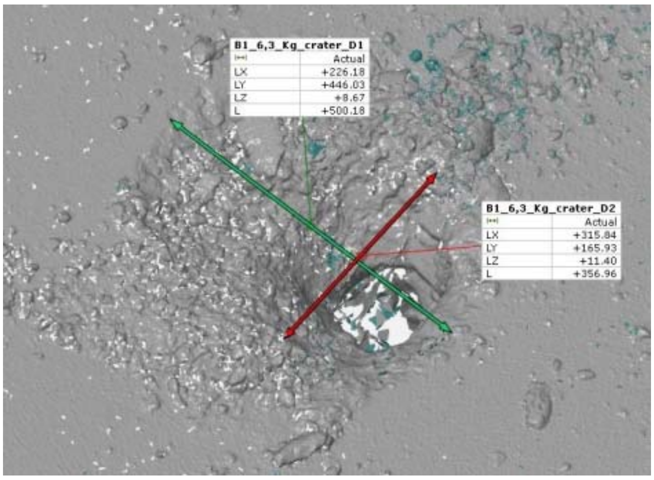

Figure 12: Crater analysis from 3D CAD geometry of Test 5.

Figure 13: Damage at the slab bottom in Test 5.

Figure 14: Hole through the whole thickness obtained in Test 5 once the crumbled concrete is removed.

It can be noted that for all the tests the blast effect is localized in an area belonging to the central preslabs where the explosion takes place. The remaining part of the structures appear undamaged. In Table 3 the dimension and shape of the craters are reported.

Craters at the slab top	Test 1 (2.1 kg)	Test 5 (6.3 kg)	Test 3 (10.5 kg)	Test 4 (10.5 kg)
Shape	Circular	Elliptical	Circular	Elliptical
Dimension	223 mm	350 mm x 500 mm	620 mm	540 mm x 610 mm

Table 3: Crater shape and dimensions.

4. Numerical Modeling

Numerical analyses were performed with the explicit finite element code LS-DYNA. Exploiting symmetries, only a quarter of the structure was modeled. Three types of Lagrangian elements were used: brick for concrete, shell for the waterproof sheet, and beam for the reinforcing steel. One of the slab edges is simply supported on a rigid surface that mimics the supporting wall. Explosive and air volume, in which the blast wave develops and propagates, were modeled with an arbitrary Lagrangian-Eulerian (ALE) technique. The fluid-structure interaction (FSI) was applied using the penalty coupling method.

Brick and shell elements are in touch, the kinematic conditions from brick to beam elements were imposed through the card CONSTRAINED_BEAM_IN_SOLID [27], while the interaction between shell and beam elements was not accounted for.

In order to compare numerical results with the measured pressure profiles, the size of the computational domain was set equal to 1810 mm x 2852 mm x 1798 mm. For those plans that are not of symmetry, non-reflecting boundary condition was adopted. Simulations were performed using a scale factor for the computed time step of 1/3 that prevents instability issues.

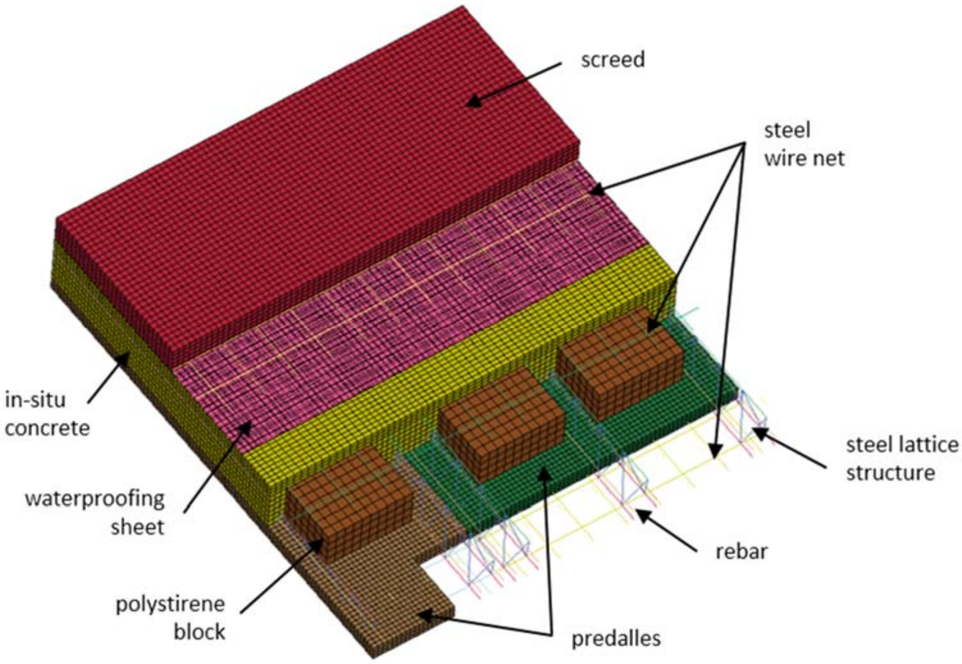

Figure 15: Slab elements discretization.

Blast wave modeling

The first step was the validation of the model of blast wave generation and propagation. The JWL equation of state (EoS) was used for the explosive [28]:

$$p_{EoS} = A\left(1-\frac{\omega}{R_1 V}\right)\exp(-\mathrm{R}_1\mathrm{V}) + \mathrm{B}\left(1-\frac{\omega}{R_2 V}\right)\exp(-\mathrm{R}_2\mathrm{V}) + \frac{\omega\mathcal{E}}{V} \tag{1}$$

where V is the relative specific volume and E the detonation energy for unit volume. In order to simulate detonation, for controlling the release of chemical energy, according to Wilkins [29] and Giroux [30], the burn fraction $F=\max(F_1,F_2)$ is introduced such that the actual pressure is:

$$p = F \times p_{EoS}\left(V,\mathcal{E}\right) \tag{2}$$

with,

$$F_1 = \begin{cases} \dfrac{2(t-t_l)DA_{e,max}}{3} & if \quad t > t_l \\ 0 & if \quad t \le t_l \end{cases} \tag{3}$$

$$F_2 = \frac{1-V}{1-V_{CJ}} \tag{4}$$

where *t* is current time, t_l the lighting time, V_{CJ} the Chapman-Jouguet relative volume, *D* the detonation velocity, $A_{e,max}$ and v_e, respectively, the maximum surface area and the volume of the generic element. The EXEM 100 physical properties and the model coefficients are reported in Table 4. Density, detonation velocity and detonation pressure were taken from the datasheet given in Table 1. The other coefficients, starting from values valid for TNT [31], were scaled in order to match the pressure profiles of the test 1 (2.1 kg of explosive).

ρ (t/mm^3)	*D* (mm/s)	P_{CJ} (MPa)	$\mathcal{E}$ (MPa)	A (MPa)	B (MPa)	R1	R2	ω (MPa)
1.27E-9	5.5E6	14300	5000	2.92E5	2.92E3	4.15	0.90	0.35

Table 4: EXEM 100 phisical properties and JWL model coefficients.

The air was model with a linear EoS:

$$p = (\gamma - 1)\frac{\rho}{\rho_0}\mathcal{E} \tag{5}$$

where $\gamma = c_p / c_v$ is the ratio of specific heats. Physical properties of the air are given in Table 5. The air model was defined through the MAT_NULL card. The pressure cut-off required to define the dilatation pressure limit was set equal to -1.0E-9 MPa.

ρ (t/mm^3)	e_0 (MPa)	c_p (J/(g K))	c_v (J/(g K))
1.23E-12	0.2533	1.006	0.7171

Table 5: Air physical properties.

Within the Eulerian mesh, the initial volume of the explosive was defined with the INITIAL_VOLUME_FRACTION option [27]. Accounting for the defined volume of the explosive, the code automatically generates a Lagrangian tetrahedral mesh.

A mesh convergence analysis was performed simulating the explosion of a single cartridge (2.1 kg) in free air. Exploiting the symmetry, the cartridge was located at the vertex of the computational domain consisting of a cube with an edge length of 1240 mm. Four different cell sizes were analyzed: 8.27, 12.4, 18.6, and 24.8 mm.

In Figure 16, the contour plot of the pressure at 575 μs on the section plane passing the middle of the cartridge is given for the different cell sizes. The coarser meshes (cell size of 18.6 and 24.8 mm) lead to an asymmetric profile for the impossibility of correctly modeling the cylindrical shape of the cartridge that has a radius of 35 mm.

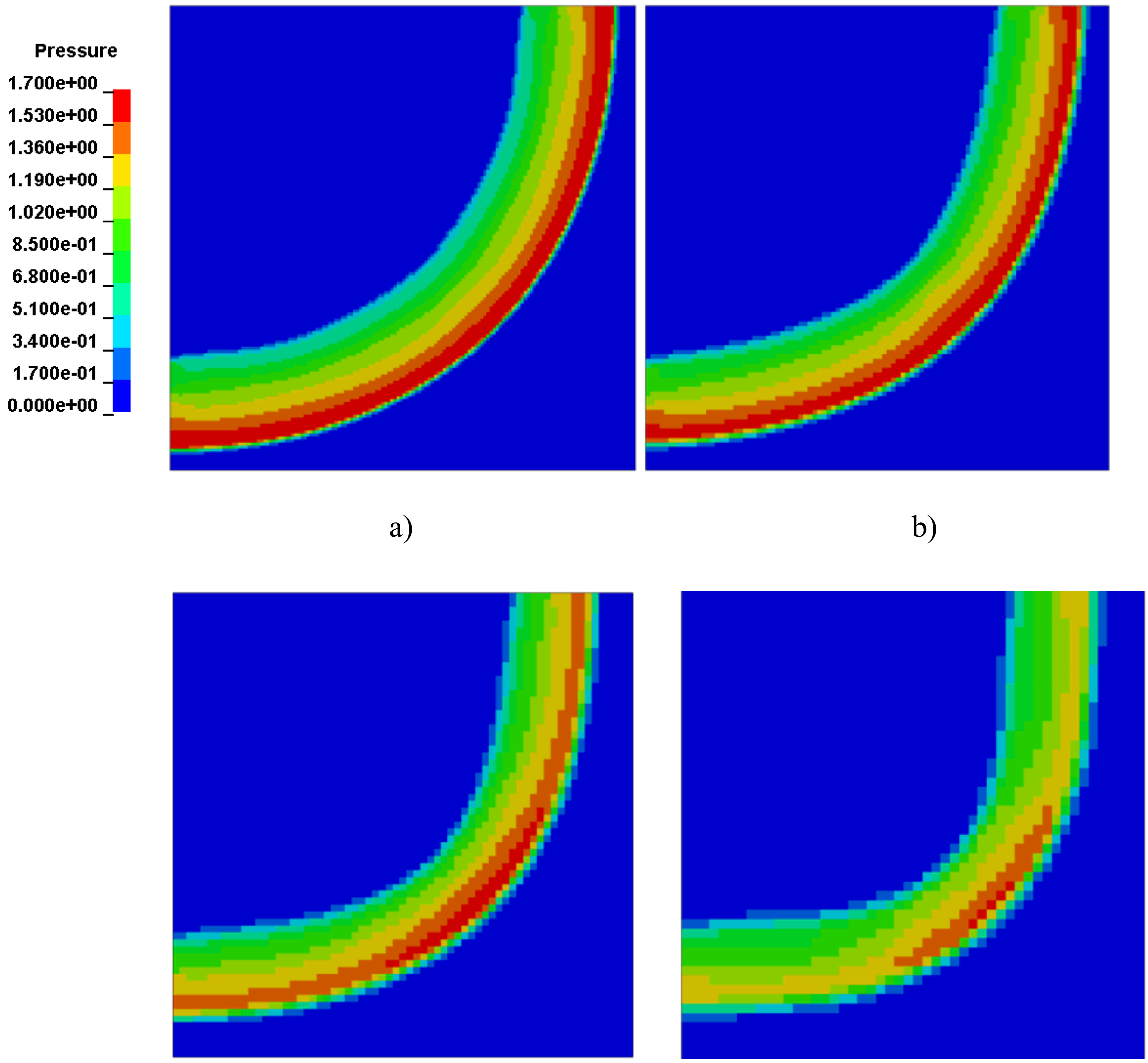

a) b)

c) d)

Figure 16: Contour plot of the pressure at 575 μs on the section plane passing the middle of the cartridge for different cell sizes: a) 8.27 mm; b) 12.4 mm; c) 18.6 mm; d) 24.8 mm.

In FIG, the peak impulses calculated at a distance of 1310 mm from the center of the cartridge, along the diagonal of the cubic computational domain are shown. Together with the values calculated for the four different cell sizes, the limit value at zero is also presented. The limit was calculated, using the three smaller values, according with [32].

The trend in Figure 17 demonstrates that a cell size of 12.4 mm allows to limit the computational costs without compromising the quality of the results and has therefore been adopted for all the other simulations.

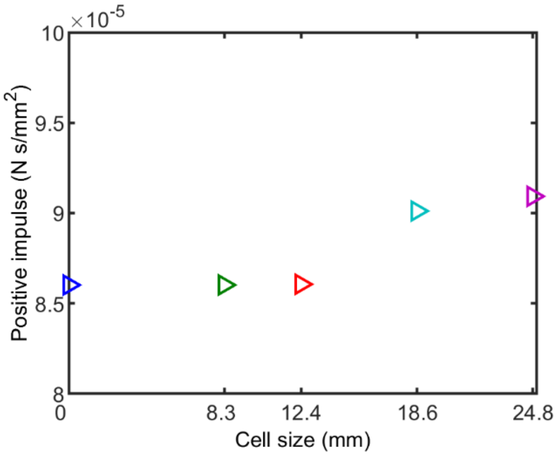

Figure 17: Peak impulses calculated for different cell sizes at 1310 mm from the the cartrige.

For the 2.1 kg configuration, the calculated profiles are compared (Figure 18) with the experimental measurements of both tests. A good agreement exists in terms of peak pressure, pressure profile, and arrival time.

Once the numerical model has been calibrated, the same set of coefficients was used to simulate the other configurations. For the 6.3 kg configuration, in order to have two symmetry planes in the numerical model, the cartridges were modeled with a single equivalent parallelepiped mass. The quarter of the modeled square cross section has a side of 53.7 mm. For 10.5 kg, each cartridge was modeled with the equivalent in mass parallelepiped geometry.

The comparisons in Figure 19 and Figure 20 show that, compatibly with the approximations made in the generation of the model, the numerical predictions agree substantially with the experimental measurements. This guarantees that, in the various configurations, the structure is correctly loaded. In the 6.3 kg configuration, the probe 2 measured a peak higher than in the case of 10.5 kg. It is not clear whether it is due to a measurement error or if the higher peak can be justified by blast wave superposition effect related to the geometry and relative position of the three cartridges. Simulation attempts have been made that have shown the possibility of obtaining such high peaks in favorable directions, but none has been able to correctly predict peak, pressure profile and arrival times of both signals simultaneously.

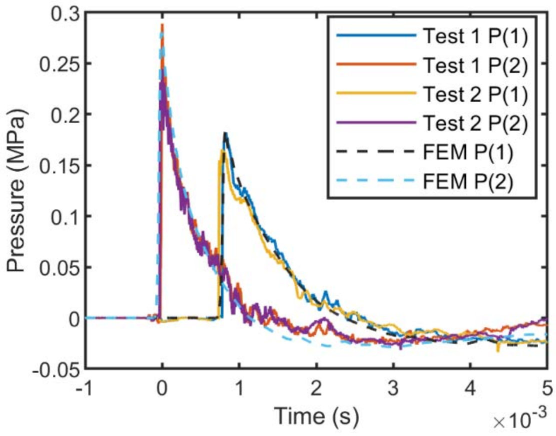

Figure 18: Comparison between measured and calculated pressure profiles for 2.1 kg of explosive.

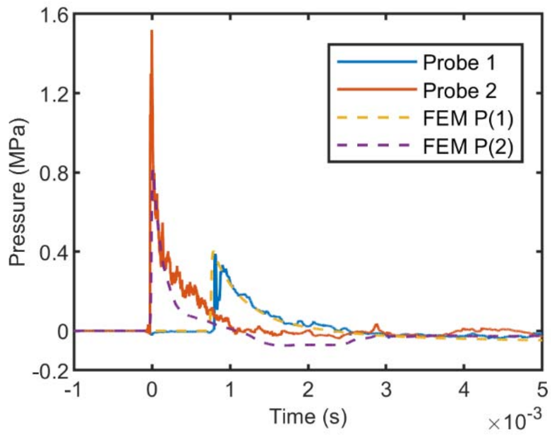

Figure 19: Comparison between measured and calculated pressure profiles for 6.3 kg of explosive.

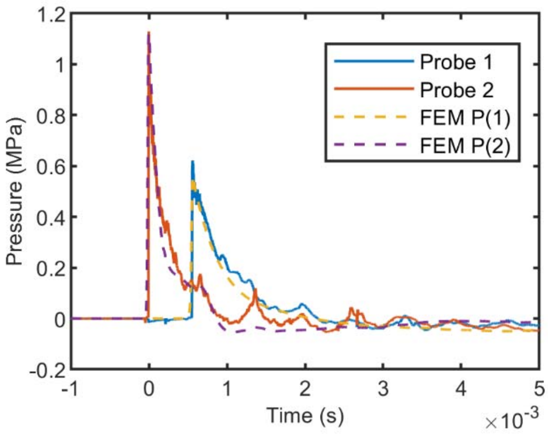

Figure 20: Comparison between measured and calculated pressure profiles for 10.5 kg of explosive.

4.1. Constitutive models for solid elements

Concrete

Mechanical behavior of concrete was described with the modeled with the Riedel-Hiermaier-Thoma (RHT) coupled damage-viscoplasticity model [33][34]. The model combines an EoS, which accounts for the porous compaction of concrete, with a strength model composed of three limit surfaces accounting for pressure, stress triaxiality and strain rate.

The model is rather complex and consists of numerous equations. Detailed descriptions can be found in [27][33][32][34][35]. It requires 38 coefficients as input in the model that has been set as follows (the notation used in the LS-DYNA manual [27] has been adopted). The following coefficients were obtained from direct measurements: RO=2.3E-6 kg/mm^3, SHEAR= 16.6 GPa, and Fc=0.040 GPa. Then, according with Ding et al. [35], to obtain a reliable description of both compressive and tension strength variations with strain rate, the following coefficients were adopted: E0C=3.0E-5 s^{-1}, E0T=1.0E-6 s^{-1}, EC=30 s^{-1}, ET=1.0 s^{-1}, BETAC=0.014, BETAT=0.031. These values have proven effective in describing correctly the behavior shown by experimental data collected from an extensive bibliography [36][37]. Specifically, they represent well the knee evident in the compressive/tension strength vs. strain rate that occurs between 10^1 and 10^2 s^{-1}, for compressive loading, and 10^0 and 10^1 s^{-1}, for tensile loading. The values of GC and GT are computed by the code in order to preserve the continuity of the compression/tension strength vs. strain rate curves. The other parameters were assumed equal to the LS-DYNA default values that can be found in [38].

A further work was made to define the coefficients for the fiber reinforced concrete that constitutes the screed. Starting from the coefficients defined above for the standard concrete, the following coefficients were calibrated on breach size and shape observed in the experiments with 2.1 kg of explosive: EC=100 s^{-1}, ET=100 s^{-1}, BETAC=0.05, BETAT=0.05, and PCO=0.8 GPa. Table of coefficients for both concretes are reported in Appendix.

Steel

The S355JR steel was used as reinforcing elements. The material was fully characterized performing quasi-static tests on smooth and round notched bars. Further, dynamic tension tests were performed with a direct tension split Hopkinson pressure bars in the strain rate range of 700 – 1500 s^{-1}. Mechanical behavior was described with the Johnson and Cook model [39] that for beam elements is available in the simplified form only [27]:

$$\sigma_y = \left(A + B\varepsilon^n\right)\left(1 + C\ln\dot{\varepsilon}^*\right) \quad (6)$$

where $\dot{\varepsilon}^* = \dot{\varepsilon} / \dot{\varepsilon}_0$ is the dimensionless plastic strain rate. The Ludwik's expression in the first set of brackets describes the strain hardening, while the expression in the second set of bracket gives the strain rate effect. The simplified model does not account for temperature and for damage effects. Thus, to model the damage evolution, an erosion criterion was adopted for which the maximum allowable stress was initially set equal to the ultimate strength (570 MPa) measured at the nominal strain rate of 1500 s^{-1}. The choice took into account that the beam element, used to model the reinforcing structures, cannot describe the onset of necking and the resulting loss of load bearing capability. However, comparison with experiments suggested that a lower value, 500 MPa, leads to results more reliable. Physical properties and model coefficients are reported in Table 6.

E (GPa)	ν	ρ (kg/m^3)	A (MPa)	B (MPa)	n	C	$\dot{\varepsilon}_0$ (s^{-1})	σ_R (MPa)
200	0.3	7800	320	705	0.354	0.011	1.0	500

Table 6: Phisical properties and JC model coefficients of the S355JR steel.

Waterproof sheets

The waterproof sheet was model with the Mooney-Rivlin model [40][41]. Since, the waterproof sheet is not a structural material, a simplified approach was adopted neglecting the strain rate and temperature effects. Thus, the strain-energy density function of the material is expressed by

$$W = A\left(I_1 - 3\right) + B\left(I_2 - 3\right) + C\left(I_3^{-2} - 1\right) + D\left(I_3 - 1\right)^2 \quad (7)$$

where,

$$C = 0.5A + B \quad (8)$$

$$D = \frac{A\left(5\nu - 2\right) + B\left(11\nu - 5\right)}{2\left(1 - 2\nu\right)} \quad (9)$$

I_1, I_2, and I_3 are the stress invariants and $2(A+B)$ is the shear modulus. The A and B material dependent coefficients were determined by an LS-DYNA inner function that performs a least square fit on tabulated stress-strain uniaxial data. The result of fitting operation is given in Figure 21. A density ρ=1000 kg/m^3 and a Poisson ratio ν=0.49 were assumed.

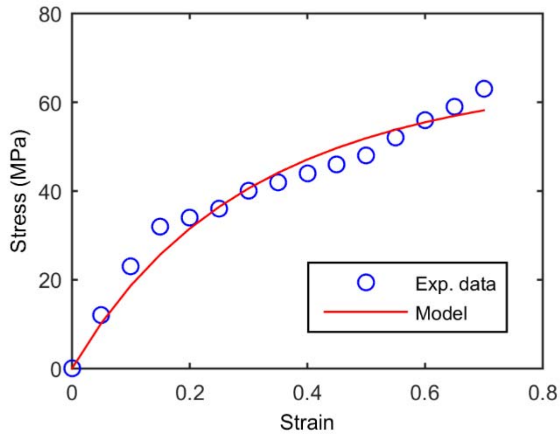

Figure 21: Stress-strain uniaxial data for the waterproof sheet.

Expanded polystyrene

Mechanical behavior of the expanded polystyrene (EPS) was described with the MAT_CRUSHBLE_FOAM material model available in LS-DYNA [27]. The model requires the setting of five coefficients: material mass density, Young's modulus, Poisson's ratio, tensile stress cutoff (TSC), damping coefficient (DAMP). In addition, the curve that describes the yield stress as a function of volumetric strain, $\gamma = 1 - V$ where V is the relative volume, has to be provided. Both coefficients (Table 7) and stress-strain curve (Figure 22) were obtained from the literature [42]. To avoid the negative volume error, which may occur at large deformation, contact interior type 2 was activated. Moreover, to account for failure in compression and to avoid excessive elements distortions, an erosion criterion was used. The limits of 0.8 for the effective plastic strain and -0.8 for the volumetric plastic strain were adopted.

E (MPa)	ν	ρ (kg/m^3)	TSC (MPa)	$DAMP$
2.2	0.0	12.5	0.1	0.5

Table 7: Coefficients of MAT_CRUSHBLE_FOAM model used for the EPS.

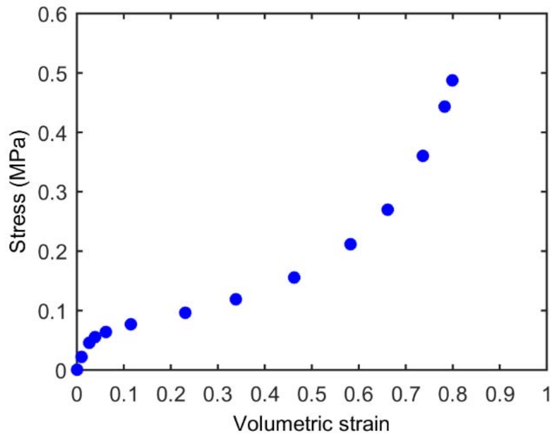

Figure 22: EPS uniaxial stress-strain curve Shah and Topa [42].

5. Numerical results

In Figure 23, the damage for the configuration with 2.1 kg of explosive, calculated after calibration of RHT model coefficients for the fiber reinforced concrete, is compared to the experimental measurements. The completely damaged elements are shown in red. On the surface, the calculated crater has a slightly elliptical geometry, with the major axis, parallel to the joist, of 240 mm and the smaller one of 200 mm, compatible with the experimental measurements that indicate an almost circular crater, with a diameter of about 223 mm. Critical damage is limited almost exclusively to the screed. It consists in crushing of concrete by porous compaction, resulting in porosity decrease, due to the compression wave on the top of the slab. Few elements reach critical damage in the in-situ concrete and some damage is present even in the preslabs.

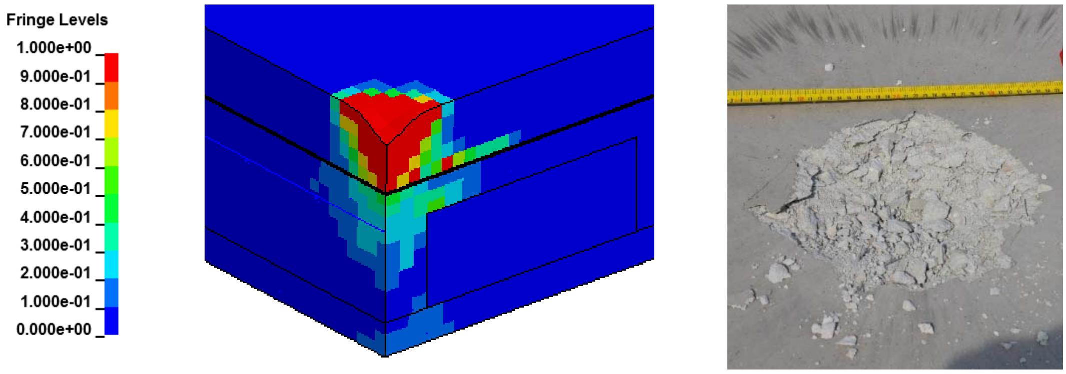

Figure 23: Damage contours and deformation for 2.1 kg of explosive compared with the experimental result.

Regarding the configuration with 6.3 kg, since three charges are adopted, a single plane of symmetry exists, and half of the structure was modeled. Consistently with what observed in the experimental test, damage affects the slab throughout the thickness, as shown Figure 24. The crater on the top of the slab has a major axis, parallel to the joist, of 400 mm and the smaller one of 320 mm; below the extrados surface, both in the screed, near the waterproof sheet and in the in-situ-concrete, the damage has a wider extension involving more material in the longitudinal direction (1240 mm) than in the transverse direction (840 mm). Damage in the upper region, as in the previous configuration, consists in pores compaction due to the compression wave. In the lower region the spalling affects a region of 642 x 410 mm^2. Spalling occurs due to the tensile wave generated by reflection at the free surface of the compression wave. These features are not visible from the damage contours of Figure 24 because, in the RHT model, the two mechanisms contribute to the same damage variable. To show the evidence of the two different damage mechanisms, pressure and damage profiles, extracted at three different positions through the slab thickness, are given in Figure 25.

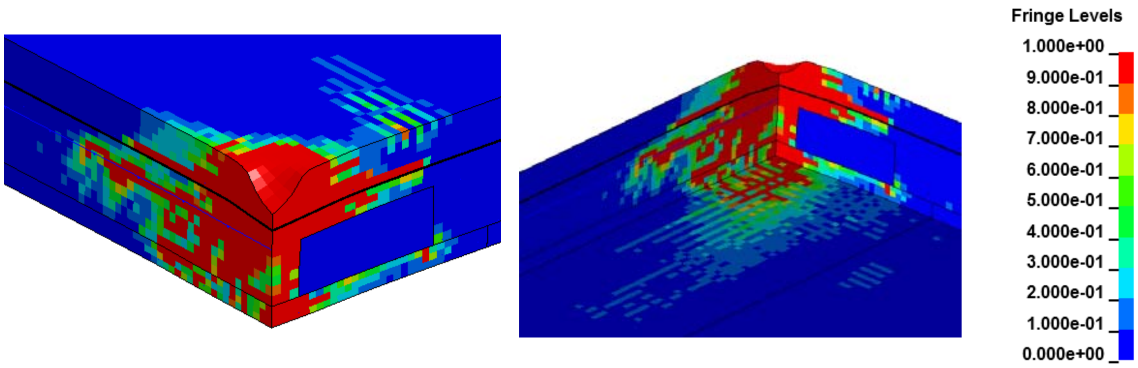

Figure 24: Damage contour for 6.3 kg of explosive.

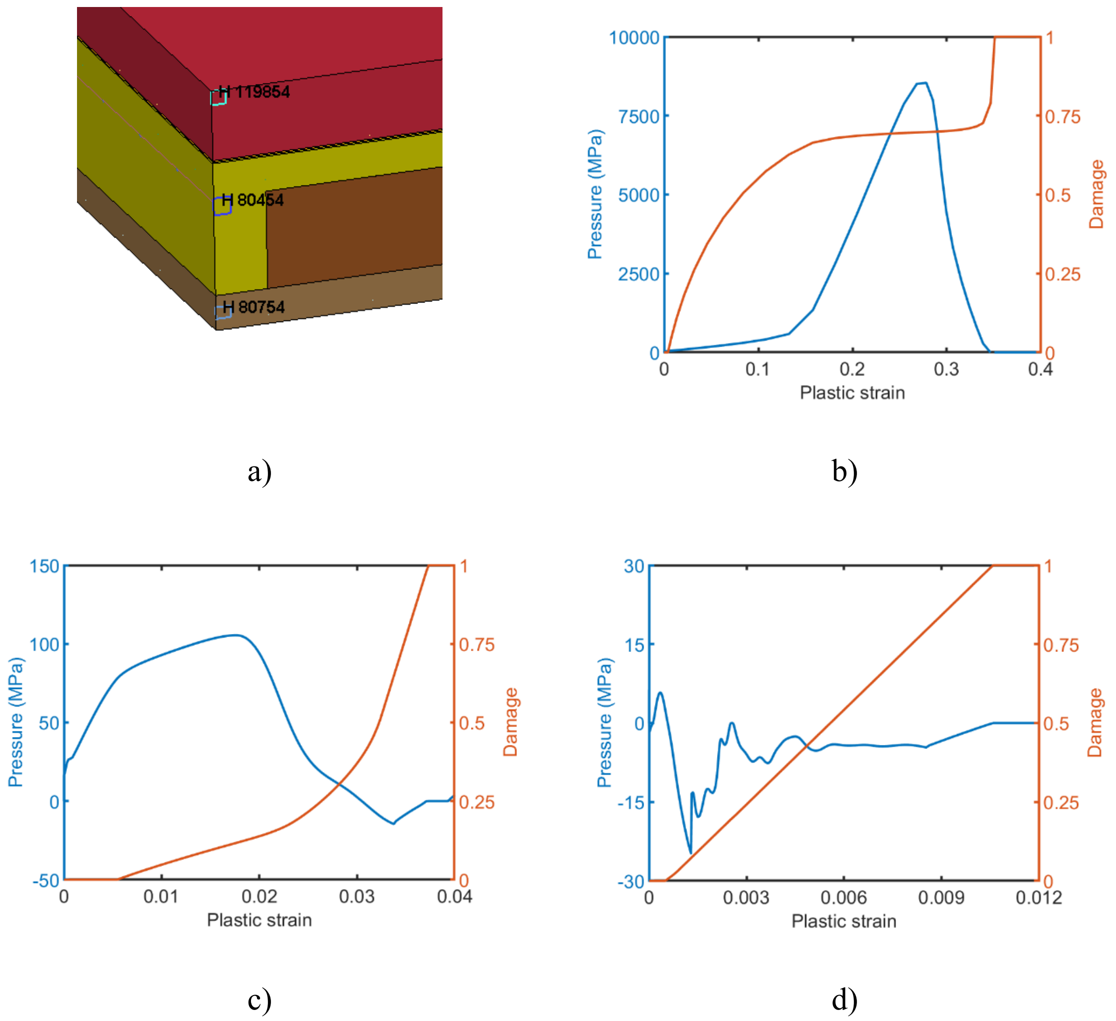

Figure 25: Pressure and damage profiles for 6.3 kg of explosive: a) positions for the extracted of profiles; b) H 119854, on the upper surface; c) H 80454, into the slab; d) H 80754, in the bottom region.

On the upper region, damage is accumulated entirely under a state of compressive strain, while in the lower region, it is accumulated in tension. In the middle, damage accumulates partially in compression and partially in tension.

The extent of the calculated damage distribution is compatible with the experimental observations of a completely crumbled concrete through the whole thickness and, at the same time, the absence of a breaching.

Failure mechanics observed for the configuration with 10.5 kg of explosive is very similar to that for 6.3 kg. However, due to the higher energy, the two failure modes lead to the breaching of the slab, as shown in Figure 26. The crater calculated on the upper surface has a circular shape with a diameter of 600 mm. In accordance with the experimental evidences, even for 10.5 kg of explosive, the damage distribution involves more material at the bottom of the slab than on the extrados, with a greater development in the longitudinal direction (1000 mm along and 680 mm orthogonally to the joist). In the middle plane the calculated damage is even more extensive (1554 mm along and 880 mm orthogonally to the joist).

Regarding the reinforcing elements, as already mentioned, the value of 570 MPa for the maximum allowable stress overestimates their strength. For 6.3 kg, no failure is predicted. For 10.5 kg, the numerical simulation correctly predicts failure occurring in wire nets of both the screed and the in-situ concrete and in the lattice structure of the joists. Yet, in contrast to the experimental observation, failure is not predicted for rebars and wire nets of the preslabs.

Assuming the lower value of 500 MPa for the maximum allowable stress of the reinforcing elements leads to more realistic prediction. In agreement with experimental results: for 6.3 kg, failure is predicted for reinforcing elements of the screed and the in-situ concrete; for 10.5 kg, failure is predicted for all elements across the thickness at the charge position.

The value calibrated in this way is well below the actual strength value measured with the material characterization. This points out a limit in the modeling of the reinforcing elements probably due to a poor representation of their plastic behavior. Besides the already discussed impossibility of describing the material post necking behavior with the beam element formulation, a further issue is the simplified form of the Johnson and Cook constitutive model adopted. This, not accounting for temperature effect on the material strength, allows a rather rough description of the steel mechanical behavior that requires a re-calibration of such coefficient.

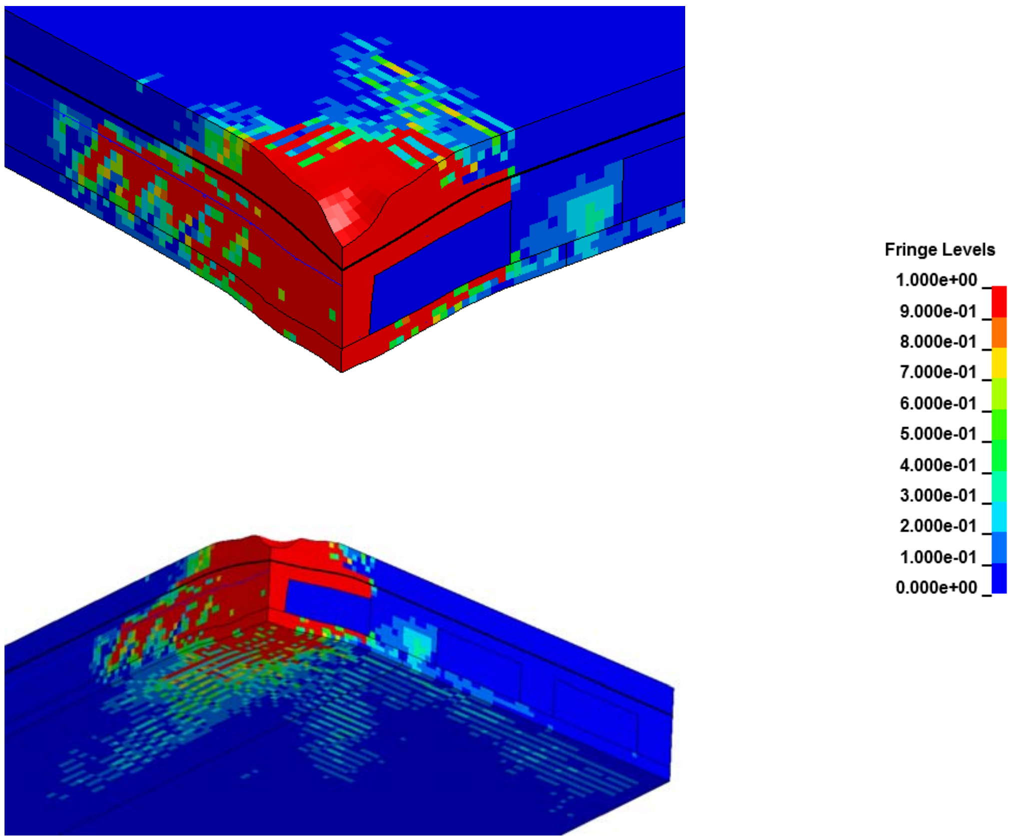

Figure 26: Damage contour for 10.5 kg of explosive.

6. Conclusions

Numerical analyses proved to be a useful tool in helping investigation where costs and security issues require limiting experimental campaigns. Here, a finite element models was developed and validated for analyzing the mechanical behavior of slab typical of civil engineering subjected to a direct contact explosion.

For the generation and the propagation of the blast wave, the ALE technique was adopted. A peculiar result is the better description of the blast wave propagation achieved meshing a rectangular volume of explosive rather than the actual cylindrical geometry. The JWL model coefficients, calibrated for the 2.1 kg of explosive, led to a good agreement between numerical and experimental pressure profiles in the other tested configurations. This guarantees their reliable use in simulations with other explosive quantities if not too far from those validated.

Validated and reliable sets of model coefficients are provided for the materials of the slab structural elements also. Specifically, the 38 coefficients of the quite complex RHT model are reported for the two types of concrete employed, the in-situ and preslabs concrete and the fiber reinforced one used for the screed.

The steel reinforcing elements were modeled with beam elements. Even if the solution is computationally very efficient, the element formulation and its implementation in LS-DYNA pose restrictions on the constitutive modeling. For this reason, an erosion criterion needed to be incorporated and conveniently calibrated.

The numerical results agree with experimental observation for all the tested configurations. For 2.1 kg of explosive, the damage occurred only in the concrete layer at the top of the slab. For 6.3 kg, even if all the slab layers resulted damaged, breaching did not occur. Damage in the upper region consisted in pores compaction due to the compression wave, while, in the lower region, spalling occurred due to the reflected tensile wave. For 10.5 kg a breach occurred but the damage remains confined in the preslabs where the cartridges are placed. For both 6.3 kg and 10.5 kg of explosive, more damage occurred in the core of the slab rather than on the top and bottom surfaces. The irregular shape of the damaged region, longitudinally elongated, can be ascribed to the inhomogeneity of the slabs that are composed of reinforced concrete, polystyrene blocks and ribs. In the slab longitudinal direction stress waves propagate unperturbed and they result accelerated by the higher stiffness due to the presence of the ribs. Instead, the low mechanical impedance of the polystyrene blocks hampers the propagation in the transverse direction. In this direction, the weakened stress wave can succeed in damaging the reduced cross section of the slab in correspondence of the polystyrene blocks, but the damage wave is stopped by the lateral ribs because of their higher strength.

It can be noted that in the test performed considering an amount of 6.3 kg of explosive, the lack of double symmetry due to the position of the three cartridges also affects the shape of the crater.

Acknowledgements: The whole experimental campaign was funded by Rete Ferroviaria Italiana that is gratefully acknowledge also for having allowed to exploit the experimental results for scientific research purposes. The GlobalSensing/CFKAD and Ing. Corrado Figuciello is gratefully acknowledge for having contributed to realize the experimental campaign and to elaborate the results.

7. References

[1] TM5-855-1, "Fundamentals of Protective Design for Conventional Weapons," US Department of the Army, Washington DC, 1987.

[2] UFC 3-340-02 "Structures to Resist the Effects of Accidental Explosions", with Change 2, 2008.

[3] Remennikov, A. Carolan, D., Building vulnerability design against terrorist attacks. In M. Stewart, B. Dockrill (Eds.), 2005.

[4] Eskew, E. and Jang, S., Impacts and Analysis for Buildings under Terrorist Attacks. Articles. 1., http://opencommons.uconn.edu/cee_articles/1, 2012

[5] Koccaz Z., Sutcu F., Torunbalci N., Architectural and structural design for blast resistant buildings. Proceedings of 14th World Conference on Earthquake Engineering October 12-17, 2008, Beijing, China.

[6] Ngo T., Mendis P., Gupta A., Ramsay J., Blast Loading and Blast Effects on Structures – An Overview. EJSE Special Issue: Loading on Structures, 76-91, 2007.

[7] Wu C., Oehlers D. J., Wachl J., Glynn C., Spencer A., Merrigan M., Day I., Blast Testing of RC Slabs Retrofitted with NSM CFRP Plates. Advances in Structural Engineering 10 (4), 397-414, 2007.

[8] Yi N. H., Kim J. H. J., Han T.S., Cho Y. G., Lee J. H., Blast-resistant characteristics of ultra-high strength concrete and reactive powder concrete. Construction and Building Materials 28, 694–707, 2012.

[9] Foglar M., Kovar M., Conclusions from experimental testing of blast resistance of FRC and RC bridge decks. International Journal of Impact Engineering 59, 18–28, 2013.

[10] Li J., Wu C., Hao H., An experimental and numerical study of reinforced ultra-high performance concrete slabs under blast loads, Materials and Design, 82, 64–76, 2015.

[11] Wang W., Zhang D., Lu F., Wang S., Tang F., Experimental study and numerical simulation of the damage mode of a square reinforced concrete slab under close in explosion. Eng. Fail. Anal. 27, 41–51, 2013.

[12] Shi Y., Chen L., Wang Z., Zhang X., Field tests on spalling damage of reinforced concrete slabs under close-in explosions. International Journal of Protective Structures 6, 389–402, 2015.

[13] Li J., Wu C., Hao H., Investigation of ultra-high performance concrete slab and normal strength concrete slab under contact explosion. Engineering Structures 102, 395–408, 2015.

[14] Zhao X., Wang G., Lu W., Yan P., Chen M., Zhou C., Damage features of RC slabs subjected to air and underwater contact explosions, Ocean Engineering 147, 531-545, 2018.

[15] Buchan P.A., Chen J. F., Blast resistance of FRP composites and polymer strengthened concrete and masonry structures – A state-of-the-art review. Composite Part B: Engineering 38, 509-522, 2007.

[16] Ohkubo K., Beppu M., Ohno T., Satoh K., Experimental study on the effectiveness of fiber sheet reinforcement on the explosive-resistant performance of concrete plates. International Journal of Impact Engineering 35, 1702-1708, 2008.

[17] Li J., Wu C., Hao H., Wang Z., Su Y., Experimental investigation of ultra-high performance concrete slabs under contact explosions. International Journal of Impact Engineering 116, 62–75, 2016.

[18] Foglar M., Hajek R., Fladr J., Pachman J., Stoller J., Full-scale experimental testing of the blast resistance of HPFRC and UHPFRC bridge decks. Construction and Building Materials 145, 588-601, 2017.

[19] Li J., Wu C., Hao H., Su Y., Experimental and numerical study on steel wire mesh reinforced concrete slab under contact explosion. Materials and Design, 116, 77–91, 2017.

[20] Yoo D.Y., Banthia N., Mechanical and structural behaviors of ultra-high-performance fiber-reinforced concrete subjected to impact and blast. Construction and Building Materials 149, 416–431, 2017.

[21] ACi370R-14 Report for the Design of Concrete Structures for Blast Effects. American Concrete Institute, 2014.

[22] Gianluca Iannitti, Nicola Bonora, Giuseppe Curiale, Stefano De Muro, Sonia Marfia, Andrew Ruggiero, Elio Sacco, Sara Scafati, Gabriel Testa Analysis of reinforced concrete slabs under blast loading. Procedia Structural Integrity, 9, 272-278, 2018.

[23] Sonia Marfia, Nicola Bonora, Giuseppe Curiale, Stefano De Muro, Gianluca Iannitti, Andrew Ruggiero, Elio Sacco, Sara Scafati, Gabriel Testa, Strengthening solutions for concrete slabs for mitigating blast effects: experimental and numerical study of full-scale frames. Submitted, 2018.

[24] UNI EN 12390-3: 2009, Prove sul calcestruzzo indurito - Parte 3: Resistenza alla compressione dei provini.

[25] UNI EN 12390-4:2002, Prova sul calcestruzzo indurito - Resistenza alla compressione - Specifiche per macchine di prova.

[26] UNI EN 12390-6:2010, Prove sul calcestruzzo indurito - Parte 6: Resistenza a trazione indiretta dei provini.

[27] LS-DYNA Keyword User's Manual, Version 971, Volume I-II, Livermore Technology Software Corporation (LSTC), May 2014.

[28] E.L. Lee, H.C. Hornig, and J.W. Kury, Adiabatic Expansion of High Explosive Detonation Products, Lawrence Livermore National Laboratory, United States1968-05-02, 1968.

[29] M.L. Wilkins, The equation of state of PBX 9404 and LX04-01, Lawrence Radiation Laboratory, Livermore, report UCRL-7797, 1964.

[30] E.D. Giroux, HEMP User's Manual, University of California, Lawrence Livermore National Laboratory, Rept. UCRL-51079, 1973.

[31] E. Lee, M. Finger, and W. Collins, JWL equation of state coefficients for high explosives, UCID-16189, Technical report, Lawrence Livermore National Laboratory, 1973.

[32] Procedure for Estimation and Reporting of Uncertainty Due to Discretization in CFD Applications, Journal of Fluids Engineering, 130 (7), 2008.

[33] W. Riedel, K. Thoma, S. Hiermaier and E. Schmolinske, Penetration of reinforced concrete by BETA-B-500, in Proceedings of the 9th International Symposiumon Interaction of the Effects of Munitions with Structures, 315-322, Berlin, 1999.

[34] W. Riedel, Beton unter dynamischen lasten meso-und makromechanische modelle und ihre parameter, PhD Thesis, Ernst-Mach-Institute, Freiburg, Germany, 2000.

[35] Y.-Q. Ding, W.-H. Tang, R.-Q. Zhang, and X.-W. Ran, Determination and Validation of Parameters for Riedel-Hiermaier-Thoma Concrete Model, Defence Science Journal; 63 (5), 2013.

[36] P.H. Bischoff and S.H. Perry, Compressive behaviour of concrete at high strain rates, Materials and Structures, 24 (6), 425-450, 1991.

[37] D.M. Cotsovos and M.N. Pavlović, Numerical investigation of concrete subjected to high rates of uniaxial tensile loading, International Journal of Impact Engineering, 35 (5), 319-335, 2008.

[38] T. Borrvall, and W. Riedel, The RHT concrete model in LSDYNA, Proceedings of the 8th European LS-DYNA Users Conference, Strasbourg, France, 2011.

[39] G.R. Johnson and W.H. Cook, A constitutive model and data for metals subjected to large strains, high strain rates and high temperatures, 7th International Symposium on Ballistics, 541-547, The Hague, The Netherlands, 1983.

[40] M. Mooney, A theory of large elastic deformation, Journal of Applied Physics, 11 (9), 582–592, 1940.

[41] R. S. Rivlin, Large elastic deformations of isotropic materials. IV. Further developments of the general theory, Philosophical Transactions of the Royal Society of London. Series A, Mathematical and Physical Sciences, 241(835), 379–397, 1948.

[42] Q.H. Shah and A. Topa, Modeling Large Deformation and failure of expanded polystyrene crushable foam using LS-DYNA, Modelling and Simulation in Engineering, 2014, Article ID 292647, 7 pages, 2014.

8. Appendix

Table 8: RHD model coefficients for in-situ and preslabs concrete.

RO	SHEAR	ONEMPA	EPSF	B0	B1	T1
(Kg/mm^3)	(GPa)					(GPa)
2.3E-6	16.6	1.0E-3	2.0	1.22	1.22	35.27

A	N	FC	FS*	FT*	Q0	B	T2
		(GPa)					
1.6	0.61	0.040	0.18	0.10	0.6805	0.0105	0.0

E0C	E0T	EC	ET	BETAC	BETAT	PTF
(s^{-1})	(s^{-1})	(s^{-1})	(s^{-1})			
3.0E-5	1.0E-6	30.0	1.0	0.014	0.031	0.001

GC*	GT*	XI	D1	D2	EPM	AF	NF
0.39	1.53	0.5	0.04	1.0	0.01	1.6	0.61

GAMMA	A1	A2	A3	PEL	PCO	NP	ALPHA0
	(GPa)	(GPa)	(GPa)	(GPa)	(GPa)		
0.0	35.27	39.58	9.04	0.0233	6.0	3.0	1.1884

719

Table 9: RHD model coefficients for the concrete of the screed.

RO	SHEAR	ONEMPA	EPSF	B0	B1	T1
(Kg/mm^3)	(GPa)					(GPa)
2.3E-6	16.6	1.0E-3	2.0	1.22	1.22	35.27

A	N	FC	FS*	FT*	Q0	B	T2
		(GPa)					
1.6	0.61	0.040	0.18	0.10	0.6805	0.0105	0.0

E0C	E0T	EC	ET	BETAC	BETAT	PTF
(s^{-1})	(s^{-1})	(s^{-1})	(s^{-1})			
3.0E-5	1.0E-6	100.0	100.0	0.05	0.05	0.001

GC*	GT*	XI	D1	D2	EPM	AF	NF
0.39	1.53	0.5	0.04	1.0	0.01	1.6	0.61

GAMMA	A1	A2	A3	PEL	PCO	NP	ALPHA0
	(GPa)	(GPa)	(GPa)	(GPa)	(GPa)		
0.0	35.27	39.58	9.04	0.0233	0.8	3.0	1.1884